

# The structural effects of (111) growth of $\text{La}_2\text{CoMnO}_6$ on $\text{SrTiO}_3$ and LSAT – new insights from 3D crystallographic characterisation with 4D-STEM and Digital Dark Field imaging

Ian MacLaren<sup>1</sup>, Andrew T. Fraser<sup>1</sup>, Matthew R. Lipsett<sup>1</sup>

1. School of Physics and Astronomy, University of Glasgow, Glasgow G12 8QQ, UK

The 3-dimensional orientation of La atom modulations has been mapped in two thin films of  $\text{La}_2\text{CoMnO}_6$  grown on  $\text{SrTiO}_3$  and LSAT ([La,Sr,Al,Ta] oxide) using a 4D-scanning transmission electron microscopy (4D-STEM) method based on the recently developed Digital Dark Field method. This images the shifts of diffraction spots and the azimuthal intensity distribution in the First Order Laue Zone, and then uses them to reconstruct and map the 3D crystallography. This clearly shows a flip from out-of-plane modulation with tensile strain on  $\text{SrTiO}_3$  to in-plane modulation with compressive strain on LSAT. This hitherto unobserved crystallographic change had a significant influence on the out-of-plane lattice parameter which left more room for the full incorporation of the larger  $\text{CoO}_6$  octahedra on LSAT and therefore explained the improved Mn-Co ordering and better properties for this film. Moreover, the method would be applicable to many other systems of epitaxial growth of complex oxides, revealing crystallographic details of crucial importance to properties which are not visible in conventional atomic resolution imaging.

## I. Introduction

Dark field imaging in the transmission electron microscope of domain orientations in functional oxides and thin films has been well used down the years [1-8], particularly to isolate specific domains based on the presence or absence of specific superlattice reflections [2,6,7]. Whilst similar information has often been obtained by atomic-resolution imaging techniques [9-14], dark field imaging has the advantage of being able to image much larger sample areas and thereby give much more statistically useful information and a better sense of the overall picture. In the case of thin epitaxial films, these may in turn reveal the crystal orientation and thus enable the characterisation of the preferred orientations (e.g. MacLaren *et al.* [2]), which can then be compared with arguments based on strain or other considerations to understand why the observed domain structure has formed. As a result, this can contribute to the optimisation of film properties by strain engineering, by growing on an appropriate substrate that gives the best domain orientations to achieve the desired properties.

In the last decade or so, dark field imaging has been extended to STEM (scanning transmission electron microscopy) using 4D-STEM techniques[15-17] (4-dimensional STEM – 2 dimensions of real space and 2 of reciprocal space) with small convergence angles such as SEND (scanning electron nanodiffraction), SPED (scanning precession electron diffraction) and other names for the same things. It has been found that arrays of apertures are especially powerful for this purpose [18-20]. Recently, we introduced a *Digital Dark Field* method based on reducing 4D-STEM datasets to a sparse list of diffraction spots (and intensities)[17,21] and then sorting them according to whether they fit to the expected positions of superlattice spots for a given domain orientation. This is especially powerful and gives much greater specificity and contrast than traditional integration of all intensity with an aperture or array of apertures.

However, the vast majority of dark field imaging carried out to-date, either in TEM or STEM, used relatively low order diffraction spots in the Zero Order Laue Zone. In other words, every study that did this is just based on the projection of the structure into a 2D-plane perpendicular to the beam direction. Whilst that has often revealed enough information for characterisation of the structures in question, it is also entirely possible that this information was incomplete because of the lack of access to the third dimension. Previously, one of the authors demonstrated the 3D connection of 60° domains in an antiferroelectric using shifts of high angle reflections in a very low angle first order Laue zone for the large unit cell in question[3], using a similar interpretation of the reciprocal lattice to Cai *et al.*[22]. However, in that study, no dark field imaging was performed using these shifted spots (nor could have been with the capabilities available at the time).

La<sub>2</sub>CoMnO<sub>6</sub> (LCMO) is a ferromagnetic semiconductor with a range of interesting properties[23] and potential applications in spintronics[24] and resistive switching devices[25]. It can either crystallise in a disordered form with Mn<sup>3+</sup> and Co<sup>3+</sup> randomly distributed among the B-sites or an ordered form where the Co<sup>2+</sup> and Mn<sup>4+</sup> ions segregate to separate interpenetrating Face Centred sublattices, akin to the well-known rock-salt structure (although actually distorted into a monoclinic cell)[26]. This latter form is the more attractive one for magnetic properties. Egoavil *et al.*[27] showed that it was possible to grow partially ordered films on SrTiO<sub>3</sub> (STO) (111) via metalorganic aerosol deposition. Later, Wang *et al.* successfully grew it on SrTiO<sub>3</sub> (STO) (001) via chemical solution methods and achieved a high degree of order. However, STO has a larger lattice parameter than LCMO so places it in tensile in-plane strain in a film. To explore the alternative direction in strain, Lv *et al.*[28] showed theoretically that growth on LaAlO<sub>3</sub>, which imposes compressive strain, changes the electronic structure and presumably properties quite markedly. Kleibecker *et al.* showed that high quality thin films of the substance can be grown on SrTiO<sub>3</sub> (STO) or LSAT (LaAlO<sub>3</sub>-Sr<sub>2</sub>TaAlO<sub>6</sub>) and that these have much better magnetic properties on (111) oriented substrates than the commonly-used (100) oriented substrates[29]. Moreover, the best properties were

achieved on LSAT where there is also compressive strain (although smaller than on  $\text{LaAlO}_3$ ). This also seemed to coincide with the longest-range ordering of Co and Mn being seen on this substrate. However, the standard STEM techniques used at the time, HAADF imaging, ABF imaging, and EELS mapping, were not capable of revealing much crystallographic information about crystallographic domains or crystal orientations although it is clear from the low symmetry crystal structure that a number of possible orientations of the monoclinic cell to the substrate would be possible and therefore domains and domain boundaries should be present. It was speculated, based on strain arguments, that  $[010]$  might prefer to lie in-plane on LSAT, but there was no evidence for this at the time.

It has long been recognised, however, that 3-dimensional information about structure and symmetry of materials is present in electron diffraction patterns at higher angles in Higher Order Laue Zone (HOLZ) rings [30,31]. Moreover, it was realised some years ago that HOLZ rings can be used in STEM imaging to bring 3D information into the images [32,33]. In recent years, this has been turned into a 4D-STEM imaging method using the intensity in a HOLZ ring to show the magnitudes of atom displacements associated with a specific crystal lattice ordering leading to a doubled periodicity *along the beam direction* [16,19,34,35]. Moreover, it was found that when a HOLZ ring arises due to back and forth atom movements along one specific direction, the intensity in the ring has a large azimuthal variation that can be fitted to reveal the direction of atom movements [36]. This approach was then applied to the LCMO film grown on LSAT by Kleibecker *et al.* [29] and it was found that the 3D displacement directions and magnitudes of the La atoms could be mapped at atomic resolution [37]. In the small areas mapped, these displacements (which should be close to  $[010]$ ) were in the interface plane, as predicted earlier by strain arguments [29].

In this work, we apply *Digital Dark Field* imaging to two thin films of LCMO grown on STO and LSAT using arrays of reflections in both the Zero and First Order Laue Zones (ZOLZ and FOLZ) together with examination of the azimuthal intensity distribution in the FOLZ. This is used to reveal a much richer picture of domain structures and their connections to substrate-induced strain than was ever imagined previously, which gives a much clearer idea of why growth on LSAT is advantageous for ordering and magnetic properties.

### A. Possible orientations of LCMO cells on (111) substrates

A (111) oriented cubic substrate will have six  $\langle 110 \rangle$  directions in-plane, all arranged at  $60^\circ$  intervals. There will be six more  $\langle 110 \rangle$  directions out of the plane, and each will be at  $60^\circ$  to two of the in-plane directions and at  $90^\circ$  to two more of them (two antiparallel directions). These will align with equivalent directions to these in the monoclinic LCMO. The equivalent directions are:

$$[100], [010], [111], [1\bar{1}1], [11\bar{1}], [1\bar{1}\bar{1}]$$

together with the negatives of these directions. It should be noted that in the  $P2_1/n$  structure, with  $a = 5.52464\text{\AA}$ ,  $b = 5.48302\text{\AA}$ ,  $c = 7.7717\text{\AA}$ ,  $\gamma = 89.898^\circ$ , the  $[100]$  and  $[010]$  are necessarily perpendicular, and therefore, one and only one of these two directions will lie in-plane. Schematics of crystallographically distinct unit cell orientations possible on this surface are shown in Figure 1b)-d), one for  $[100]$  in-plane, and two for  $[010]$  in-plane, using the colour scaling on Figure 1a), which shows the relative lengths of the different vectors (and a comparison to substrate vector lengths). Note that  $[111]/[1\bar{1}1]$  and  $[11\bar{1}], [1\bar{1}\bar{1}]$  have different lengths because LCMO is monoclinic so there is a real difference between the arrangements in Figure 1 c) and d) (even if the strain difference would be pretty small). However, Figure 1b) is the only possibility for  $[100]$  in-plane, as it always means a flip from a  $\langle 111 \rangle$  to a  $\langle \bar{1}\bar{1}\bar{1} \rangle$  for the other two in-plane directions. These different possibilities will be crucial in interpreting the structures revealed in the Results below.

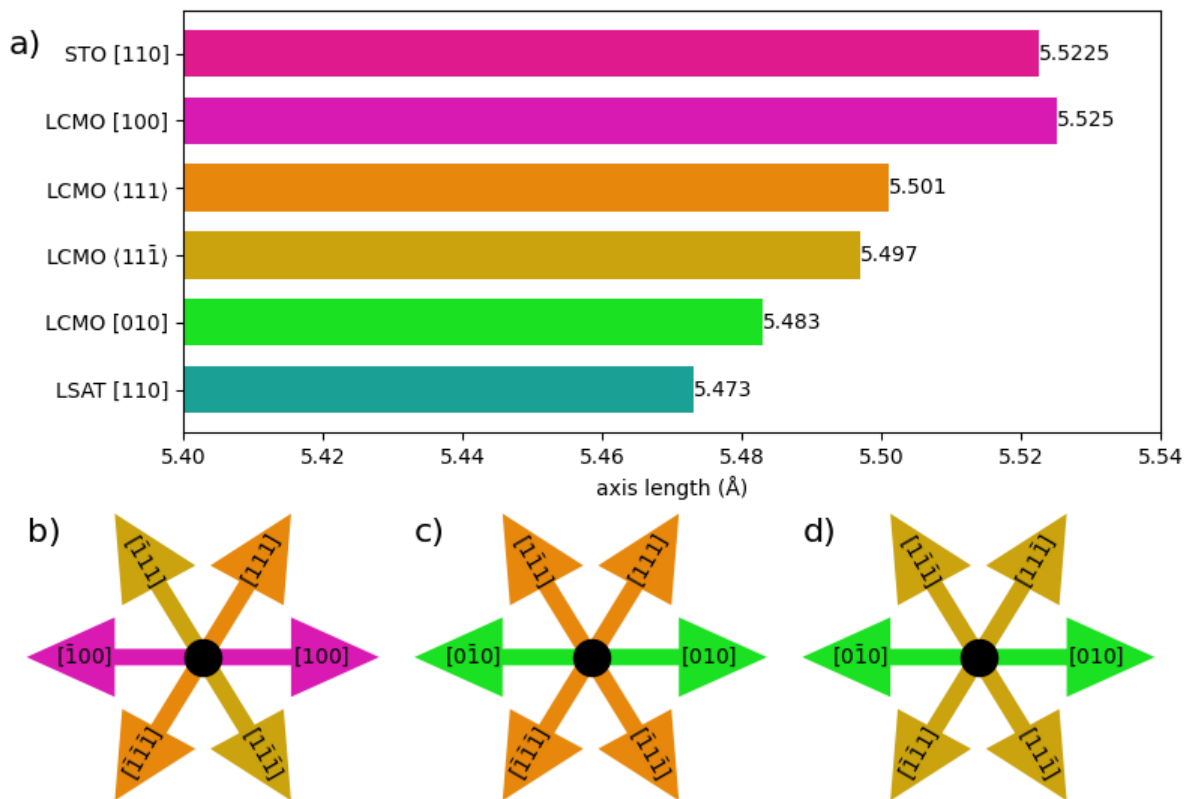


Figure 1: a) Lengths of different monoclinic axes equivalent to cubic perovskite  $[111]$  compared with the substrate vectors, and b)-d) Schematics of some different possible arrangements of these vectors of the monoclinic LCMO structure on a  $(111)$  surface of cubic perovskite, the colours of the arrows correlates to the colour scale in part a). Whilst other specific sets of indices are possible, these are the only three symmetrically distinct possibilities: b) **a**-axis in-plane ( $[01\bar{1}]$  normal); c) and d) **b**-axis in-plane ( $[10\bar{1}]$  and  $[\bar{1}0\bar{1}]$  normals).

## II. Methods

The samples were grown on (111) substrates of STO and LSAT by pulsed laser deposition from prepared targets of  $\text{La}_2\text{CoMnO}_6$  with full details in our previous publication[29]. Samples for electron microscopy were prepared by standard FIB liftout protocols.

Scanning transmission electron microscopy was performed using a JEOL ARM200F operated at 200 kV in TEM mode using the smallest spot size (5) and the smallest condenser aperture (10  $\mu\text{m}$ ) to produce the lowest convergence angle beam available. Scanning precession electron diffraction (SPED) datasets were acquired over suitable areas of film and substrate using a NanoMEGAS TopSpin system using a Quantum Detectors MerlinEM system for the diffraction pattern acquisition with a single 256 $\times$ 256 pixel Medipix-3 detector. For diffraction patterns containing higher order Laue zones, a short camera length of 30 cm was chosen to ensure the full angular range was seen on the detector, and a very small precession angle of 0.1 $^\circ$  was selected to allow some of the benefits of precession in getting more uniform diffraction disks, whilst not mixing the different Laue zones (which happens at higher precession angles). In one case, a larger camera length of 80 cm was used to see more detail of the ZOLZ with a precession angle of 0.5 $^\circ$ . All SPED data was exported as .app5 files and converted to .hdf5 using Gary Paterson's *fpd* software[19].

The main 4D-STEM data processing was performed with py4DSTEM[17] (0.4.18), including determination of list of diffraction peak positions (aka *pointslists*), determination of pattern centres, determination of lattice vectors for the perovskite lattice using the *strain* functions, and the Digital Dark Field imaging. All experimental diffraction patterns were plotted after rotation (with *scipy.ndimage*) to compensate for the calibrated rotation angle between the scanned image and diffraction (a calibration formula was previously determined using a  $\text{MAG}^*\text{I}^*\text{CAL}$  specimen[38] between a rotated scan of arbitrary scan rotation and the diffraction pattern orientation). Thus, any feature in any experimental diffraction pattern could be directly related to the spatial orientations of features in its partner image. Determination of the azimuthal modulation in the FOLZ from a list of diffraction spots was performed using an adapted version of the fitting previously published by Silinga *et al.*[36] written in python and using *scipy.optimize.curve\_fit*. A full code listing is provided in the data deposit accompanying this paper. The reconstruction and visualisation of the 3D orientations of the La-displacements was performed with standard python/numpy/matplotlib functions. Dynamical simulation of diffraction patterns was performed using *py4dstem*, which uses a Bloch wave method. Full code is provided in the data deposit.

### III. Results

#### A. Diffraction pattern simulations to aid interpretation

Figure 1 shows simulations of 6 diffraction patterns from directions equivalent to  $\langle 110 \rangle_{\text{cubic}}$  (technically, there are another 6 equivalent directions, which are the negatives of these). Two are for the principal lattice directions  $[100]$  and  $[010]$  (Figure 1a) and 1b)), and show no lower angle First Order Laue zone, but only a higher angle one at about  $3.8\text{-}3.9 \text{ \AA}^{-1}$ . However, the other four (Figures 1c)-f)) have low angle First Order Laue zones at about  $2.7 \text{ \AA}^{-1}$ . The symmetry reduction and increase in cell size means that none of these four has twofold symmetry or any true mirrors, once we consider the full pattern including the Higher Order Laue Zones [31]. The shift of pattern origin in this structure with  $a \approx b \approx \sqrt{2}a_{\text{cubic}}, c \approx 2a_{\text{cubic}}$  is approximately:

$$\mathbf{g}_B = h_B k_B l_B = \frac{Nu}{4} \frac{Nv}{4} \frac{Nw}{2} \text{ for } \mathbf{B} = [uvw] \quad [1]$$

where  $\mathbf{g}_B$  is a direction in reciprocal space, expressed in Miller indices, parallel to the beam direction,  $\mathbf{B}$ , expressed as a normal real-space vector.  $\mathbf{g}_B$  is given with a magnitude equal to the spacing between the  $0^{\text{th}}$  and  $N^{\text{th}}$  reciprocal lattice layers, and the relationship between the indices of parallel real and reciprocal space vectors is the normal one based on the standard definitions of  $\mathbf{a}^*$ ,  $\mathbf{b}^*$  and  $\mathbf{c}^*$  in terms of  $\mathbf{a}$ ,  $\mathbf{b}$  and  $\mathbf{c}$ , the basis vectors for the unit cell in real space. So, for example,  $[111]$  gives  $\mathbf{g}_B = \frac{1}{4} \frac{1}{4} \frac{1}{2}$  for the centre of the FOLZ. This means that  $\frac{1}{4}$  shifts are going to be found along  $\langle 112 \rangle$  directions, but these could be either up or down, depending on the rotational orientation of the diffraction pattern. Figures 1c)-f) show different choices for the  $\langle 112 \rangle$  direction, always pointing downwards in the figure. For 1d) and 1f), the  $\frac{1}{4}$  shift follows this  $\langle 112 \rangle$  direction, whereas in 1c) and 1e) it is antiparallel, which can be expressed as  $-\frac{1}{4}$  or  $\frac{3}{4}$  (the latter choice is made in this work). This shift of spots in the FOLZ with respect to the ZOLZ is clearly linked to the direction of the crystallographic  $\mathbf{b}$ -axis. In each case, the direction in which  $[010]$  or  $[0\bar{1}0]$  is pointing out of the page towards the reader is shown with an orange arrow (the beam direction out of the page towards the reader is given in every subfigure title). In all cases, if the  $\frac{1}{4}$  shift downwards is present,  $\mathbf{b}$  is pointing up somewhere in the upper half of the pattern. If the  $\frac{3}{4}$  shift is present,  $\mathbf{b}$  is pointing up somewhere in the lower half of the pattern.

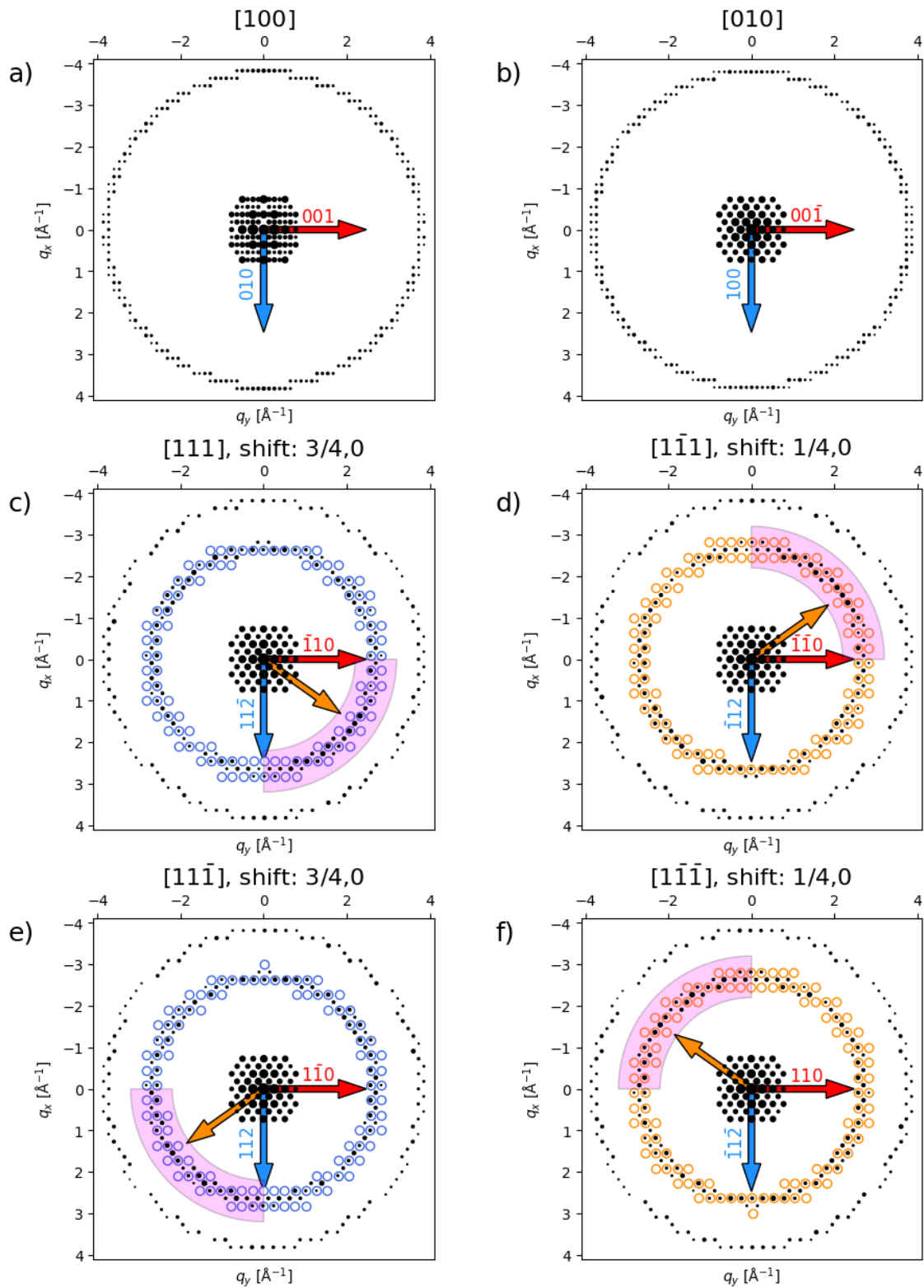


Figure 2: Dynamical simulations of diffraction patterns for six distinct orthorhombic directions equivalent to  $\langle 110 \rangle_{\text{cubic}}$  for a crystal thickness of 50nm. In each case the directions of  $\mathbf{g}_1$  (vertical, blue) and  $\mathbf{g}_2$  vectors (horizontal, red) are arrowed with indices (although absolute length is magnified to make the arrows easy to see). Five of the six

have similar ZOLZ patterns; the latter four have an inner FOLZ. The shift of the rectangular lattice of the ZOLZ to the pattern is shown, either a  $\frac{1}{4}$  shift downwards (and FOLZ reflections circled in orange) or a  $\frac{3}{4}$  shift downwards (equivalent to a  $\frac{1}{4}$  shift upwards, and FOLZ reflections circled in blue). The direction in which the **b**-axis of the structure points upwards out of the page is shown with an orange arrow. The brightest quadrant of the FOLZ is highlighted in pink.

To compare with our recent publications where the intensity modulation in the FOLZ was fitted [36] and then used to determine the absolute direction of **b** at atomic resolution [37] (actually **d**, displacement vector, but close to **b**), the brightest quadrant was determined and indicated in pink. For the thickness used in the simulation, this was always the same quadrant as contained the **b** axis pointing up out of the page. However, further investigation as shown in Figure S1 of the Supplementary Information shows that the contrast modulation is thickness dependent – at some thicknesses, the brightest quadrant is the opposite one to that containing the **b** axis pointing up out of the page. Thus, whilst mapping the azimuthal modulation is useful, determining the absolute sign of direction works by combining the directional peak of modulation (which narrows it down to two quadrants) and the direction of the  $\frac{1}{4}$  shift (which then narrows it down to one). This, therefore, gives a method for determining the direction of the **b**-axis from nanobeam diffraction patterns. Firstly, we can map the direction of the shift using Digital Dark Field Imaging [39]. Secondly, we can map the peak modulation direction using the azimuthal fitting algorithm used previously [36], albeit adapted for datasets that are discrete lists of diffraction spot positions and intensities from disc detection applied to nanodiffraction [39] (aka *pointslists* [17,21]) rather than a continuous intensity distribution to get the peak intensity direction. These two pieces of information can then be combined to map out the directions of the **b**-axis in 3D.

The angles between  $\mathbf{g}_1$  and  $\mathbf{g}_2$  are given in Table 1 for each of the diffraction patterns of Figure 2, and this information is useful in later discussion and interpretation of experimental results.

<b>B</b>	$\mathbf{g}_1$	$\mathbf{g}_2$	Angle (°)
[100]	020	002	90.00
[010]	200	00 $\bar{2}$	89.90
[111]	11 $\bar{2}$	$\bar{1}10$	89.74
[1 $\bar{1}1$ ]	$\bar{1}12$	$\bar{1}\bar{1}0$	90.26
[11 $\bar{1}$ ]	112	1 $\bar{1}0$	90.36
[1 $\bar{1}\bar{1}$ ]	$\bar{1}\bar{1}\bar{2}$	110	89.64

Table 1: Angles between the basis vectors for each of the diffraction patterns of Figure 2.

## B. Digital Dark Field Imaging of the Film grown on LSAT

Figure 3 shows Digital Dark field (DDF) images and corresponding diffraction patterns from a few areas in a thin film grown on LSAT. Figure 3a) shows an image formed with

just a rectangular array of primitive perovskite reflections in the ZOLZ; together with the corresponding diffraction pattern for the image position indicated with a white spot, with red ring overlays for each diffraction spot position included in the summation. This image should therefore highlight all perovskite areas with the same crystal orientation. Most areas of both film and substrate are bright in this image, as one would expect for an epitaxial perovskite film on a perovskite substrate. The top of the image area is dark as this is either carbon or deposited platinum and is not imaged by this array of dark field apertures. There is a dark area to the lower right, which is probably a CoO inclusion, as noted previously [29]. There is also a general intensity gradient from brighter on the left to less bright on the right, which is simply from a thickness gradient in the specimen (which causes more intensity to be scattered outside of coherent diffraction spots).

Figure 3b) shows an image formed with a rectangular array of “apertures” in the ZOLZ with a  $\frac{1}{2}, \frac{1}{2}$  shift of the origin to pick up the superlattice spots expected for the orientations shown in Figure 2b-f), together with the corresponding diffraction pattern with magenta overlays indicating the aperture positions. Again, almost all areas of the film and substrate appear bright with this set of reflections, indicating they are present for any and all domains of both substrate and film in this sample orientation. Again, the only obvious exception is the CoO inclusion to the lower right. However, one area of the film to the left-hand side is much brighter than everywhere else in the film. This is the area from which the diffraction pattern was extracted, and it can be clearly seen that there is no inner FOLZ and a fairly bright set of  $\frac{1}{2}, \frac{1}{2}$ -shifted reflections in the ZOLZ. This corresponds with expectations for [010] as shown in Figure 2b). The fact that Figure 3b) is bright in patches of the substrate indicates that this is not a primitive perovskite for the most part, but has some additional unit cell ordering leading to the appearance of this superlattice spot – this would certainly be expected in  $\text{LaAlO}_3$ , which LSAT is based upon.

However, most areas of the film do contain an additional inner FOLZ ring. Figure 3c) is made for FOLZ reflections with a shift of  $\frac{3}{4}, 0$  and  $\frac{1}{4}, \frac{1}{2}$  (these correspond to the primitive array of spots and the  $\frac{1}{2}, \frac{1}{2}$ -shifted array of superlattice spots in the ZOLZ, all with a  $\frac{3}{4}, 0$  shift applied for the FOLZ). (The positive shift directions are left-down / right-down in all diffraction patterns). The location from which the exemplar diffraction pattern is extracted is shown with a white dot, with the array of aperture positions shown in orange. Clearly there is a strong ring in the diffraction pattern and two particular areas of the film are seen in the image that are bright, which must be domains with a specific orientation related to one of Figures 2c)-f). The substrate is dark in Figure 3c).

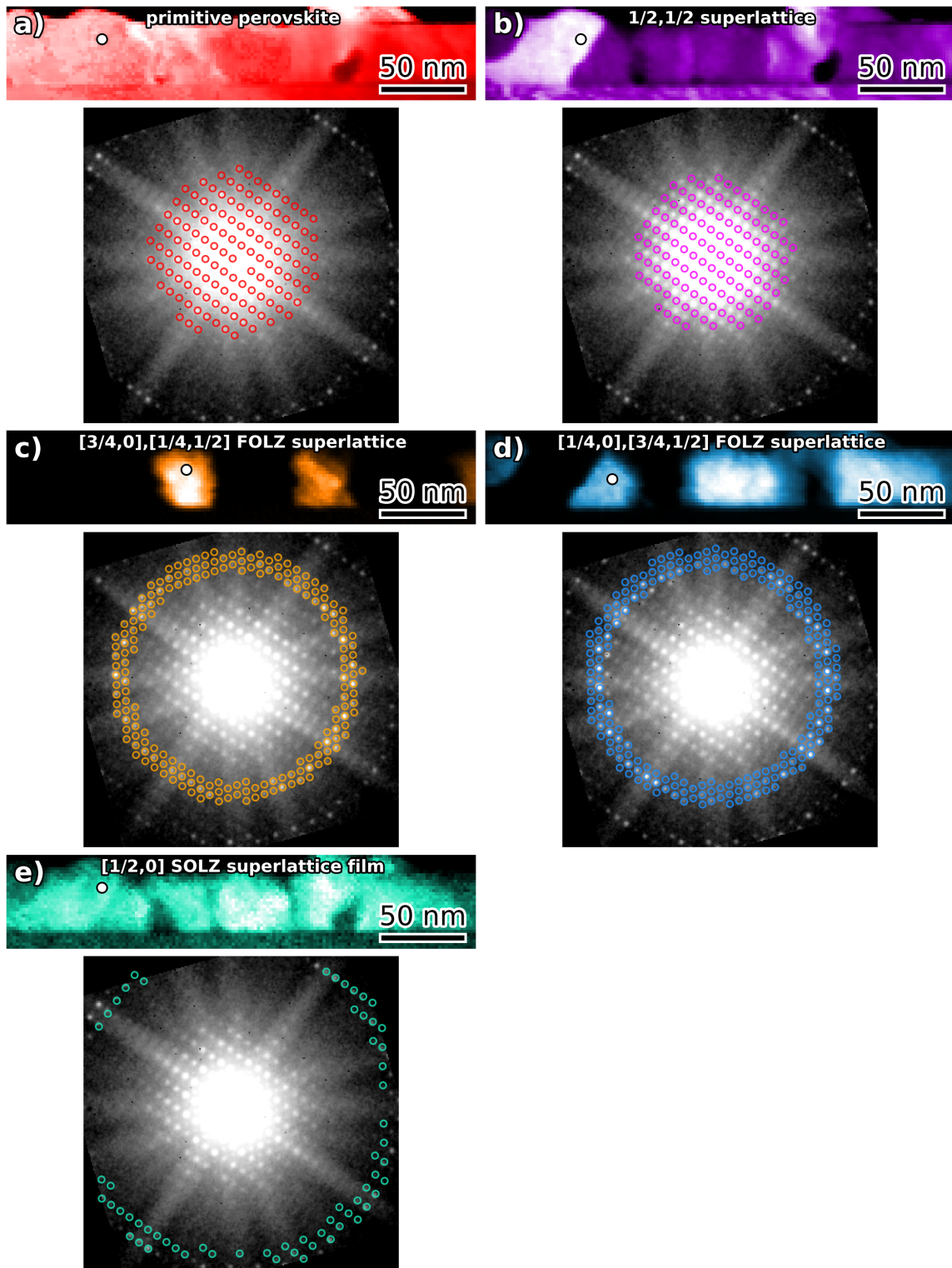


Figure 3: Digital Dark Field (DDF) Images and corresponding exemplar diffraction patterns with overlays for the DDF apertures from the LCMO film grown on LSAT for: a) primitive perovskite reflections; b) reflections shifted by  $\frac{1}{2}, \frac{1}{2}$  in the ZOLZ; c) reflections shifted by  $\frac{3}{4}, 0$  and  $\frac{1}{4}, \frac{1}{2}$  in the FOLZ; d) reflections shifted by  $\frac{1}{4}, 0$  and  $\frac{3}{4}, \frac{1}{2}$  in the FOLZ; e) reflections shifted by  $\frac{1}{2}, 0$  in the outer Laue zone (SOLZ for  $\langle 111 \rangle$  or  $\langle 11\bar{1} \rangle$ ).

Similarly, Figure 3d) is made for FOLZ reflections with a shift of  $\frac{1}{4},0$  (corresponding to the primitive array in the ZOLZ) and  $\frac{3}{4},\frac{1}{2}$  (corresponding to the superlattice of  $\frac{1}{2},\frac{1}{2}$ -shifted array in the ZOLZ). The location from which the exemplar diffraction pattern was extracted is shown with a white dot. The array of aperture positions is shown in cornflower blue on the diffraction pattern. Again, the FOLZ ring is strong and several bright areas of film the film are seen in the image, corresponding to specific domains. And as for Figure 3c), the substrate is dark. So, this inner FOLZ is only present in the film.

It should also be noted that the brightest parts of the FOLZ ring for both Figures 3c) and 3d) are to the left and right of the rotated diffraction patterns, indicating a **b**-axis in the plane of the specimen, which is also consistent with the single  $[010]$  domain seen in Figure 3b). The frequent reversal between  $\frac{3}{4},0$  and  $\frac{1}{4},0$  orderings suggests that the 3D orientation of this **b**-axis rotates frequently in the plane of the film between successive domains, but a full 3D rendering will be calculated below.

Figure 3e) was made with a set of apertures corresponding to the SOLZ ( $\frac{1}{2},0$  shift) for the  $\langle 111 \rangle$  or  $\langle 11\bar{1} \rangle$  directions (equivalent to the FOLZ for the primitive perovskite structure or for the  $[100]$  or  $[010]$  directions). All film domains light up in this image, and the diffraction pattern is shown with green-blue overlays for the apertures. The substrate was mostly dark in this image and there is little sign in the substrate diffraction patterns of any strong Laue zone– which is probably a result of significant local compositional disorder in the LSAT. A similar effect was seen previously for  $\text{La}(\text{Sr},\text{Mn})\text{O}_3$  [34].

One final note is that the two **g**-vectors for constructing the lattice of aperture positions were optimised for every DDF image (i.e. the vectors were adjusted by a simple routine to minimise the RMS deviation of the aperture positions from the experimentally measured array of spots) and the angles between them measured afterwards. It doesn't much matter if this is done in the ZOLZ or FOLZ, the results tend to correlate to  $<0.1^\circ$ . For the spot marked in Figure 3b) in the  $[010]$  domain, the angle is measured as  $90.0^\circ$ , in pretty good agreement with expectations of  $89.9^\circ$ , as in Table 1. For the spot marked in Figure 3c), it is  $90.5^\circ$ , which is larger than the  $90.24^\circ$  expected for a  $\langle 111 \rangle$  or  $90.36^\circ$  expected for a  $\langle 11\bar{1} \rangle$ . For the spot marked in Figure 3d), it is  $90.8^\circ$ , which is even further from expectations. It would seem likely from this evidence that though we have something like the symmetry of the bulk structure and the zone axes are quite identifiable, it seems likely that the lattice parameters are a bit more distorted from cubic than in the bulk, possibly not dissimilar to in our previous work on  $\text{LaFeO}_3$  grown on a  $(111)$  substrate [35].

### C. Digital Dark Field Imaging of the Film grown on STO

Figure 4 shows DDF images and their corresponding diffraction patterns for the LCMO film grown on STO, and the same figure parts are calculated with the same arrays of apertures for Figures 4a)-d) to those used for Figures 3a)-d). Figure 4a) is a DDF image for an array of spots in the ZOLZ corresponding to primitive perovskite and this lights up both film and substrate, as expected. Figure 4b) shows a DDF image calculated for ZOLZ reflections for a  $\frac{1}{2}, \frac{1}{2}$  shifted array, which is superlattice spots only seen for the orientations simulated in Figure 2b)-f). This lights up most of the film (save a patch in the centre) but none of the substrate. The substrate not lighting up is no surprise as it should be simple cubic  $\text{SrTiO}_3$  with no superlattice spots at all. Figure 4c) shows a DDF image from the FOLZ for the  $\frac{3}{4}, 0$  shift. Unlike for the film on LSAT, the  $\frac{1}{4}, \frac{1}{2}$  shifted array was not calculated as such spots seemed extremely weak or invisible. This is possibly a sign of a further subtle structural alteration from the bulk structure. This shift lights up the vast majority of the area lit up in Figure 4b). Figure 4d) shows a DDF image from the FOLZ for the  $\frac{1}{4}, 0$  shift and in this case, only a tiny triangular notch is lit up with this particular shift. Again, the second array to go with this,  $\frac{3}{4}, \frac{1}{2}$  was not calculated as spots in this array are weak to invisible in the diffraction patterns.

Whilst superlattice spots in the ZOLZ with  $0, \frac{1}{2}$  shifts could be discerned by eye in this diffraction dataset, they were so close to the much brighter primitive perovskite spots that automated peak detection was not reliable. Thus, a dataset at a longer camera length used in our previous work [39] was used to make this image, and after a little cropping and correction of drift distortion in that dataset, this is shown in Figure 4e). This clearly demonstrates that the central domain of the film is  $[100]$  oriented.

The outer Laue Zone (SOLZ for  $\langle 111 \rangle$  or  $\langle 11\bar{1} \rangle$ ) was generally weak in this dataset so was not used for making a DDF image, unlike in Figure 3e).

As for angles between basis vectors, it is  $89.9^\circ$  in the  $\text{SrTiO}_3$  substrate, which is in good agreement with the expected  $90^\circ$ . At the white dot in Figures 4a) and 4b), this angle is  $89.4^\circ$  and values in the range  $89.4^\circ$ - $89.6^\circ$  are found throughout the bright areas in Figure 4c) (i.e. areas with the  $\frac{3}{4}, 0$  shift). As for the film on LSAT, these values are further from  $90^\circ$  than expected suggesting larger distortion in the film than in the bulk structure. In marked contrast to this, the little notch of  $\frac{1}{4}, 0$  shift has an angle of  $90^\circ$ , suggesting that this has deformed in the opposite sense for some reason.

As for peaks of intensity in the FOLZ, this appears to be somewhere round about  $100$ - $110^\circ$  and  $280$ - $290^\circ$  ACW from horizontal right (which is the consistent definition in this paper for  $0^\circ$ ) for the  $\frac{3}{4}, 0$  shift area in Figure 4c), suggesting a **b**-axis orientation not in the film plane (and therefore **a** in-plane). One  $[100]$  domain is also seen which agrees with this. However, for the triangular domain of Figure 4d), the peak intensity lies around  $0^\circ$  /  $180^\circ$ , suggesting **b**-axis in-plane.

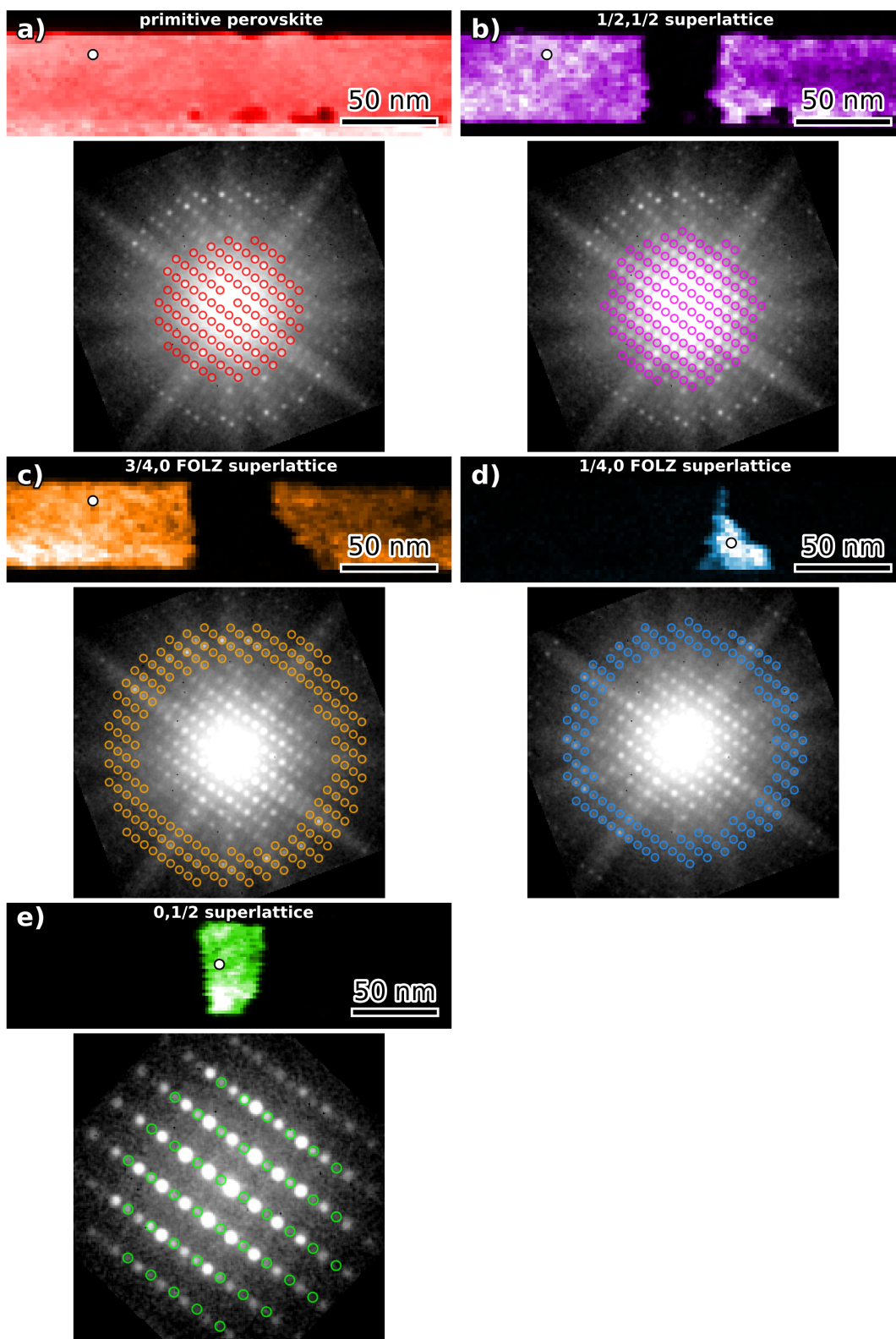


Figure 4: Digital Dark Field (DDF) Images and corresponding exemplar diffraction patterns with overlays for the DDF apertures from the LCMO film grown on STO for: a) primitive perovskite reflections; b) reflections shifted by  $1/2, 1/2$  in the ZOLZ; c) reflections shifted by  $3/4, 0$  in the FOLZ; d) reflections shifted by  $1/4, 0$  in the FOLZ; e) DDF image and

diffraction pattern from a different dataset at a different camera length on this area for reflections shifted by  $0, \frac{1}{2}$  in the ZOLZ.

### D.3D crystal orientations – reconstruction, reasons and consequences

Combining the information encoded in the DDF images from the FOLZ showing the direction of the  $\frac{1}{4}$  shift, and the information from fitting the azimuthal intensity variation, it is possible to construct 3D colour maps of **b**-axis orientation. Figure 5 shows this reconstruction for the film grown on LSAT, and the clear tendency is to form fairly equiaxed domains of the order of 50 nm in size, all with the **b**-axis in-plane, whether red (up-right), cyan (up-left) or white (parallel to beam direction).



Figure 5: 3D orientations of **b**-axes in the LCMO film grown on LSAT. The colour scale indicates 3D orientation in the upper hemisphere (out of the page), and the arrows are superimposed to make this even more unambiguous.

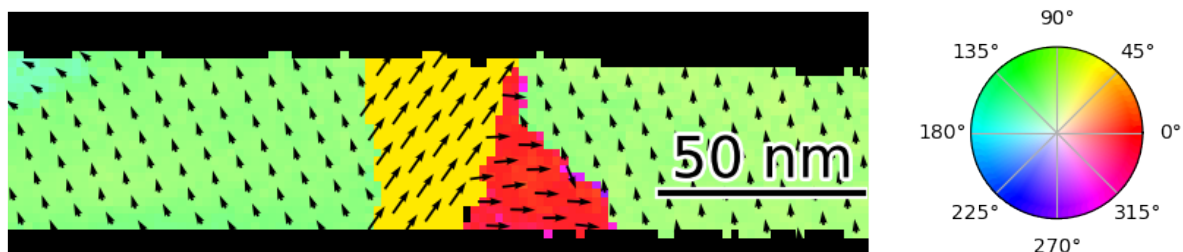


Figure 6: 3D orientations of **b**-axes in the LCMO film grown on STO. The colour scale indicates 3D orientation in the upper hemisphere (out of the page), and the arrows are superimposed to make this even more unambiguous.

Figure 6 shows the same reconstruction for the film grown on STO. In this case, the clear tendency of the **b**-axes to line up in directions out of the film plane (technically, at  $\sim 71^\circ$  to film plane) is seen, although there is the one anomalous area where the **b**-axis has lined up parallel to film plane in the red notch. Quite why no arrows pointing at about  $290^\circ$  and out of the page are seen is unclear, as it would seem that this **b**-axis orientation should be equally likely if **b** tends to point out-of-plane. Perhaps it is the case that the domains are relatively large, and such domains may be elsewhere in the film. Certainly, the density of domain boundaries seems smaller than in the LSAT film for some reason. Maybe the strains caused by domain formation out-of-plane would lead to highly strained domain boundaries which could disfavour that formation.

Now the reason for this change in preferred crystal orientation between the two substrates is fairly clear when one considers the differences in lattice parameters, as summarised in Figure 1a). For growth on STO, most of the possible equivalents to  $[110]_{\text{cubic}}$  for LCMO are slightly short, except for  $\langle 100 \rangle$ . So, the lowest strain option is  $\langle 100 \rangle$ ,  $\langle 111 \rangle$  and  $\langle 11\bar{1} \rangle$  (Figure 1b)). This is the preference seen in Figure 6, although one minority area has nucleated a  $\langle 010 \rangle$  in-plane. It is unclear why this is the case, but maybe strain from surrounding domains stabilised an unusual strain state at this junction. There are additional clues in the strain map shown in Figure S2, where there is little difference in horizontal strain ( $\epsilon_{yy}$  for this set of axis definitions) from film to substrate, but a slight negative strain (i.e. compressive) out-of-plane. This suggests that there is a weak strain effect from substrate to film in this case, and once the domain structure above has been formed, this is sufficient to accommodate most of the strain.

For growth on LSAT, however, whichever of the possible equivalents to  $[110]_{\text{cubic}}$  is in-plane, these directions would all be slightly long and the film will be in compressive strain in-plane, possibly with some compensatory out-of-plane expansion[40]. This is borne out in the strain maps shown in Figure S3, where the out-of-plane strain is strongly positive (around 1.0-1.5%). The lowest strain set of vectors in-plane from Figure 1 would be  $\langle 010 \rangle$ ,  $\langle 11\bar{1} \rangle$  and  $\langle 11\bar{1} \rangle$  (Figure 1d)), closely followed by  $\langle 010 \rangle$ ,  $\langle 111 \rangle$  and  $\langle 111 \rangle$  (Figure 1c)). This is exactly the preference seen in Figure 5. Distinguishing  $\langle 111 \rangle$  or  $\langle 11\bar{1} \rangle$  could not be reliably done at this time, especially considering that the monoclinic distortion seems characteristically stronger than in the bulk refinement [26]. However, the angle between vectors in the strain maps seems consistently less than  $90^\circ$  throughout the majority of the film, which would be in accordance with positive strain out-of-plane.

In this respect, it turns out that these films are like many oxide thin films grown before, in that the dominant effect on domain selection is strain (for instance MacLaren *et al.*[2]), and it is rare that this is not the case (a recent example was published where strain was small and oxygen octahedral coupling played a significant role[41]). However, unlike most previous studies, where simple diffraction in the ZOLZ or contrast in atomic resolution imaging were able to resolve the domain orientations and link them to film-substrate strain, this case gave no hints in atomic resolution STEM imaging[29] and little unambiguous information in the ZOLZ of diffraction patterns. Only the occasional area oriented along  $[100]$  gives an unambiguous diffraction pattern, and that is just a minority of areas in the film grown on STO.

So, the question remains as to why growth on LSAT should give better Co-Mn ordering than growth on STO[29]. If we have  $[100]$  in-plane, then the film plane is either  $(011)$  or  $(01\bar{1})$ . These have a lattice spacing of  $4.48 \text{ \AA}$  in the bulk[26] and that might be slightly lower still with the compressive out-of-plane strain of about -0.5-0.75% seen in this film. On the other hand, if we have  $[010]$  in-plane, the film plane is either  $(101)$  or

( $10\bar{1}$ ), which have plane spacings of 4.51 or 4.50 Å in bulk. Using the LSAT as a reference, then the out-of-plane strain is between 1.0 and 1.5%, and that corresponds to actual out-of-plane lattice parameters of 4.51-4.54 Å. With the benefit of hindsight, this does accord with Figure 2 of Kleibecker *et al.* [29] where the out-of-plane lattice parameter for LCMO on STO is clearly smaller than that for LSAT. This difference might not sound much, but might make all the difference in atomic ordering. To get perfect atomic ordering, we need alternate layers of Mn and Co filling the B sites. Whilst Mn<sup>4+</sup> is relatively small, Co<sup>2+</sup> is relatively large (Bull *et al.* [42] found Mn-O distances of 1.89 Å and Co-O distances of 1.99 Å in ordered LCMO). Thus, the promotion of a crystal orientation that allows bigger spaces out-of-plane, and then increases the size of those spaces further with a little tensile strain in the same direction is going to be really favourable for creating layers that have enough space to fit the Co atoms in in a complete layer.

It is particularly enlightening that the presence or absence of the low angle FOLZ ring and the precise details of both the shift of diffraction spots in this ring and the azimuthal intensity variation around this are so rich in information. It is therefore interesting to wonder if there were ambiguities of interpretation in previous studies which were not resolved because of not having access to this information. For example, Woodward and Reaney [43] produced an excellent survey of the appearance of different families of superlattice spots in perovskites with different octahedral tilt systems, but unambiguous determination always depended on extensive tilting because it only used the ZOLZ. Heavy tilting is both time consuming even when possible, and impractical in thin films with small domains where overlaps of neighbouring domains will be a problem at higher tilts. In contrast to this, the new 4DSTEM methodology accomplishes this 3D crystallographic characterisation over a significant area of film in a single scan and with processing that can readily be automated now it has been demonstrated. As such, this can become a very powerful tool for the characterisation of complex oxide heterostructures and thereby invaluable in the development of oxide based functional devices.

## IV. Conclusions

We have performed Digital Dark Field Imaging of thin films of La<sub>2</sub>CoMnO<sub>6</sub> films grown by pulsed laser deposition on SrTiO<sub>3</sub> and LSAT, using sets of superlattice reflections in the zeroeth, first, and second order Laue zones. The 3-dimensional information in the higher order Laue zones is much more specific and informative than just using the zeroeth order Laue zone alone, as has been standard practice in most dark field imaging to date. The azimuthal distribution of intensity in the first order Laue zone could also be determined. By combining the information in the different Laue zones, and using simulations of different diffraction patterns, it was possible to determine the 3D orientation of the La displacements in the crystal structure in a simple automated way.

Thus, domain structures and crystal axes of the monoclinic structure were visualised in terms of 3D orientations of the **b**-axis, and this revealed a huge difference between STO, in which case the **b**-axis preferred to sit out of the film plane (approximately 71° to the film plane) and LSAT, in which the **b**-axis preferred to sit in the film plane. This was explained on the basis of the switch from tensile strain on STO to compressive strain in LSAT. Moreover, this switch to growth on a substrate that gives compressive in-plane strain creates a larger out-of-plane lattice spacing on LSAT, giving more room to fit in the larger CoO<sub>6</sub> octahedra, and thus promoting stronger Co-Mn ordering, which ultimately gives better properties. More generally, the methods herein would allow similar 3D characterisation of crystal orientations in other heteroepitaxial functional oxide systems where domain structures may play a strong role in driving the properties and performance.

## Acknowledgements

This work was only possible as a result of what was started by EPSRC funding of the grant “Fast Pixel Detectors: a paradigm shift in STEM imaging” (EP/M009963/1), and funded the computer server used in the calculations. Prof. Judith L. MacManus Driscoll and Dr. Josée Kleibeuker at the University of Cambridge are thanked for the provision of the films used in this work. IM is grateful to Prof Colin Ophus of Stanford University for helpful discussions, especially as regards making the dynamical simulations used in Figure 2.

## References

- [1] A. C. Daykin and C. J. Kiely, *Philos. Mag. A* **68**, 1331 (1993).
- [2] I. MacLaren, Z. L. Wang, H. S. Wang, and Q. Li, *Philos. Mag. A* **82**, 1405 (2002).
- [3] I. MacLaren, R. Villaurrutia, and A. Peláiz-Barranco, *J. Appl. Phys.* **108**, 034109 (2010).
- [4] I. MacLaren, T. Ras, M. MacKenzie, A. J. Craven, D. W. McComb, and S. De Gendt, *J Electrochem Soc* **156**, G103 (2009).
- [5] W. Y. Wang, Y. L. Zhu, Y. L. Tang, Y. B. Xu, Y. Liu, S. Li, S. R. Zhang, Y. J. Wang, and X. L. Ma, *Appl. Phys. Lett.* **109**, 202904 (2016).
- [6] J. C. Jiang, X. Q. Pan, and C. L. Chen, *Appl. Phys. Lett.* **72**, 909 (1998).
- [7] Y. L. Li, L. Q. Chen, G. Asayama, D. G. Schlom, M. A. Zurbuchen, and S. K. Streiffer, *J. Appl. Phys.* **95**, 6332 (2004).
- [8] S. Kitagawa, T. Ozaki, Y. Horibe, K. Yoshii, and S. Mori, *Ferroelectrics* **376**, 122 (2008).
- [9] C. J. Lu, Z. L. Wang, C. Kwon, and Q. X. Jia, *J. Appl. Phys.* **88**, 4032 (2000).
- [10] O. I. Lebedev, J. Verbeeck, G. V. Tendeloo, S. Amelinckx, F. S. Razavi, and H. U. Habermeier, *Philos. Mag. A* **81**, 2865 (2001).
- [11] C. L. Jia, S. B. Mi, K. Urban, I. Vrejoiu, M. Alexe, and D. Hesse, *Nat. Mater.* **7**, 57 (2008).
- [12] R. J. Zeches *et al.*, *Science* **326**, 977 (2009).

- [13] C. T. Nelson *et al.*, *Nano Lett.* **11**, 828 (2011).
- [14] H. W. Zandbergen, S. Freisem, T. Nojima, and J. Aarts, *Phys. Rev. B* **60**, 10259 (1999).
- [15] C. Ophus, *Microsc. Microanal.* **25**, 563 (2019).
- [16] I. MacLaren, T. A. Macgregor, C. S. Allen, and A. I. Kirkland, *APL Mater.* **8**, 110901 (2020).
- [17] B. H. Savitzky *et al.*, *Microsc. Microanal.* **27**, 712 (2021).
- [18] V. B. Ozdol, C. Gammer, X. G. Jin, P. Ercius, C. Ophus, J. Ciston, and A. M. Minor, *Appl. Phys. Lett.* **106**, 253107 (2015).
- [19] G. W. Paterson, R. W. H. Webster, A. Ross, K. A. Paton, T. A. Macgregor, D. McGrouther, I. MacLaren, and M. Nord, *Microsc. Microanal.* **26**, 944 (2020).
- [20] S. J. McCartan, I. Calisir, G. W. Paterson, R. W. H. Webster, T. A. Macgregor, D. A. Hall, and I. MacLaren, *J. Am. Ceram. Soc.* **104**, 2388 (2021).
- [21] C. Ophus, S. E. Zeltmann, A. Bruefach, A. Rakowski, B. H. Savitzky, A. M. Minor, and M. C. Scott, *Microsc. Microanal.* **28**, 390 (2022).
- [22] Y. Cai, F. Phillipp, A. Zimmermann, L. Zhou, F. Aldinger, and A. Ruhle, *Acta Mater.* **51**, 6429 (2003).
- [23] H. Wang, J. Gazquez, C. Frontera, M. F. Chisholm, A. Pomar, B. Martinez, and N. Mestres, *NPG Asia Materials* **11**, 44 (2019).
- [24] C. Meyer, V. Roddatis, P. Ksoll, B. Damaschke, and V. Moshnyaga, *Phys. Rev. B* **98**, 134433 (2018).
- [25] F. Lv, Y. Qin, Y. Gao, F. Huang, H. Tang, J. Liu, L. Long, and Y. Yang, *Materials Today Communications* **36**, 106454 (2023).
- [26] C. L. Bull, H. Y. Playford, K. S. Knight, G. B. G. Stenning, and M. G. Tucker, *Phys. Rev. B* **94**, 014102 (2016).
- [27] R. Egoavil, S. Hühn, M. Jungbauer, N. Gauquelin, A. Béché, G. Van Tendeloo, J. Verbeeck, and V. Moshnyaga, *Nanoscale* **7**, 9835 (2015).
- [28] S. Lv, Z. Wang, M. Saito, and Y. Ikuhara, *J. Appl. Phys.* **113** (2013).
- [29] J. E. Kleibeuker *et al.*, *NPG Asia Materials* **9**, e406 (2017).
- [30] P. M. Jones, G. M. Rackham, and J. W. Steeds, *Proc. R. Soc. London Ser. A-Math. Phys. Eng. Sci.* **354**, 197 (1977).
- [31] J. P. Morniroli and A. Redjaimia, *J. Microsc.-Oxf.* **227**, 157 (2007).
- [32] J. C. H. Spence and C. Koch, *Philos. Mag. B* **81**, 1701 (2001).
- [33] F. T. Huang, A. Gloter, M. W. Chu, F. C. Chou, G. J. Shu, L. K. Liu, C. H. Chen, and C. Colliex, *Phys. Rev. Lett.* **105**, 125502, 125502 (2010).
- [34] M. Nord, J. Barthel, C. S. Allen, D. McGrouther, A. I. Kirkland, and I. MacLaren, *Ultramicroscopy* **226**, 113296 (2021).
- [35] M. Nord, A. Ross, D. McGrouther, J. Barthel, M. Moreau, I. Hallsteinsen, T. Tybell, and I. MacLaren, *Phys. Rev. Mater.* **3**, 063605 (2019).
- [36] A. Silinga, C. S. Allen, J. Barthel, C. Ophus, and I. MacLaren, *Microsc. Microanal.* **29**, 1682 (2023).
- [37] I. MacLaren, A. Silinga, J. Barthel, J. E. Kleibeuker, J. L. MacManus-Driscoll, C. S. Allen, and A. I. Kirkland, *arXiv e-prints*, 2412.16297 (2024).
- [38] J. P. McCaffrey and J. M. Baribeau, *Microsc. Res. Tech.* **32**, 449 (1995).
- [39] I. MacLaren, A. T. Fraser, M. R. Lipsett, and C. Ophus, *Microsc. Microanal.* **31**, ozae104 (2025).
- [40] I. MacLaren, Z. L. Wang, H. S. Wang, and Q. Li, *Appl. Phys. Lett.* **80**, 1406 (2002).

- [41] D. T. L. Alexander, H. Meley, M. M. Schmitt, B. Mundet, J.-M. Triscone, P. Ghosez, and S. Gariglio, *ACS Nano* **19**, 10126 (2025).
- [42] C. L. Bull, D. Gleeson, and K. S. Knight, *J. Phys.-Condens. Mat.* **15**, 4927 (2003).
- [43] D. I. Woodward and I. M. Reaney, *Acta Crystallogr. Sect. B-Struct. Commun.* **61**, 387 (2005).

# The structural effects of (111) growth of $\text{La}_2\text{CoMnO}_6$ on $\text{SrTiO}_3$ and LSAT – new insights from 3D crystallographic characterisation with 4D-STEM and Digital Dark Field imaging

## Supplemental Materials

Ian MacLaren<sup>1</sup>, Andrew T. Fraser<sup>1</sup>, Matthew R. Lipsett<sup>1</sup>, Josee Kleibeuker<sup>2,3</sup>, Judith L. Driscoll<sup>2</sup>

1. School of Physics and Astronomy, University of Glasgow, Glasgow G12 8QQ, UK
2. Department of Materials Science & Metallurgy, University of Cambridge, 27 Charles Babbage Road, Cambridge CB3 0FS, UK
3. DEMCON high tech systems Eindhoven BV, Kanaaldijk 29, 5683 CR Best, The Netherlands

## Effect of thickness on intensity distribution in the FOLZ and determining **b**-axis orientation

Figure S1 shows a set of 6 simulations of [111] diffraction patterns for thicknesses from 20 nm to 120 nm. The intensity distribution in the FOLZ does show some changes with thickness, and the integrated intensity for each quadrant is calculated for each and ranked in order with highlights in red (most intense), yellow, green and blue (least intense) being used to show which is which. It is clearly seen that the brightest quadrant changes with thickness, but it is only a swap between red and yellow in top-left, bottom-right and vice versa. A similar effect is seen with blue-green in top-right, bottom-left. This is effectively a normal dynamical diffraction effect where details of intensity distribution may vary with thickness. Thus, just using the brightest quadrant to determine the absolute 3D orientation of **b** is not feasible. However, the geometry of the patterns is unaffected by thickness, as would also be expected. The peak azimuth is always in either the top-left or bottom-right quadrant, so accurately showing the 2D projected direction of the **b**-axis reliably. And the shift of spots in the FOLZ with respect to ZOLZ is consistent throughout at  $\frac{3}{4}, 0$  (those corresponding to  $\frac{1}{2}, \frac{1}{2}$  spots in the ZOLZ are not circled for clarity). This then provides a consistent way of direction in which **b** is pointing in 3D. A  $\frac{3}{4}, 0$  shift always correlates with the **b**-axis pointing up in the lower half of the figure. Putting together that the direction has to be lower right or upper left AND has to be lower, then means that lower right is the direction in which the **b** axis comes up out of the page. The same works for all  $\langle 111 \rangle_{\text{monoclinic}}$  directions in whichever in-plane orientation is shown.

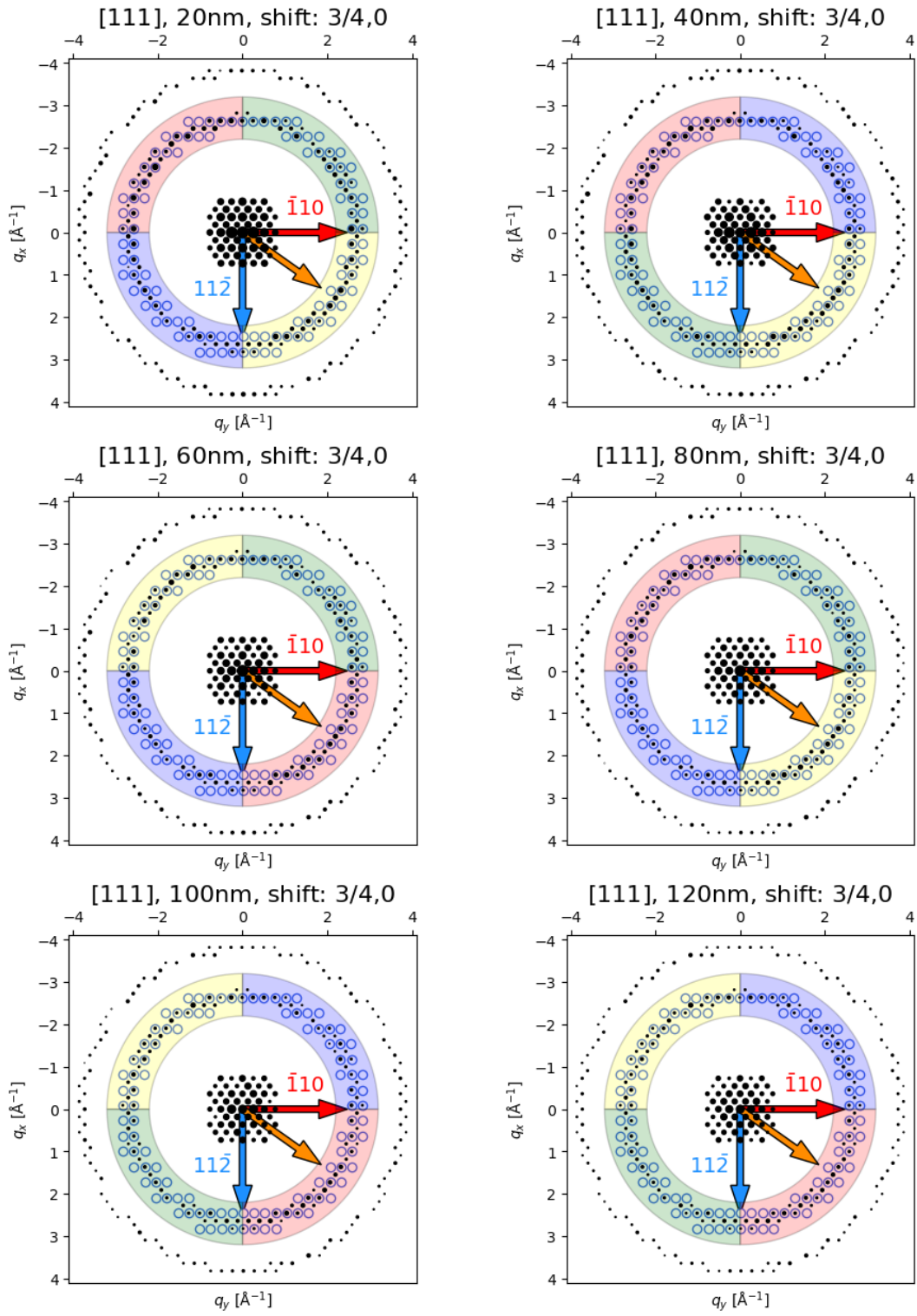


Figure S1: Dynamical simulations of the same diffraction pattern for six different thicknesses. The quadrants of the FOLZ are highlighted in order of summed intensity: red (most intense), yellow, green, blue (least intense). The direction in which the  $\mathbf{b}$ -axis of the structure points upwards out of the page is shown with an orange arrow. The brightest quadrant of the FOLZ is highlighted in pink.

## Strain measurement in the two datasets

Figures S2 and S3 show strain mapping applied to the two datasets using py4dstem. Out-of-plane is the most significant strain direction as it is the direction that is free of constraint. And the angle between the basis vectors (deviation from 90°) also shows significant trends.

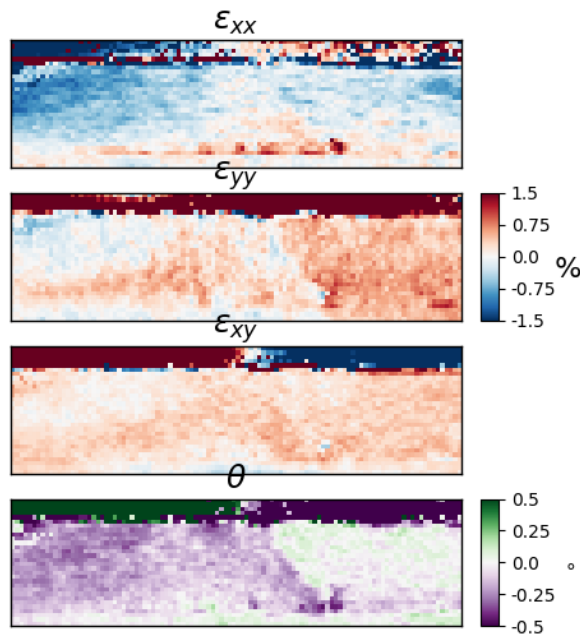


Figure S2: Strain maps for the LCMO film on STO for in ( $\epsilon_{yy}$ ) and out of plane ( $\epsilon_{xx}$ ) using vectors aligned with the image axes. There is slight out-of-plane compressive strain here. The left-hand-side seems to have a negative deviation from perpendicular vectors ( $<90^\circ$ ), and the right hand side is close to  $90^\circ$ .

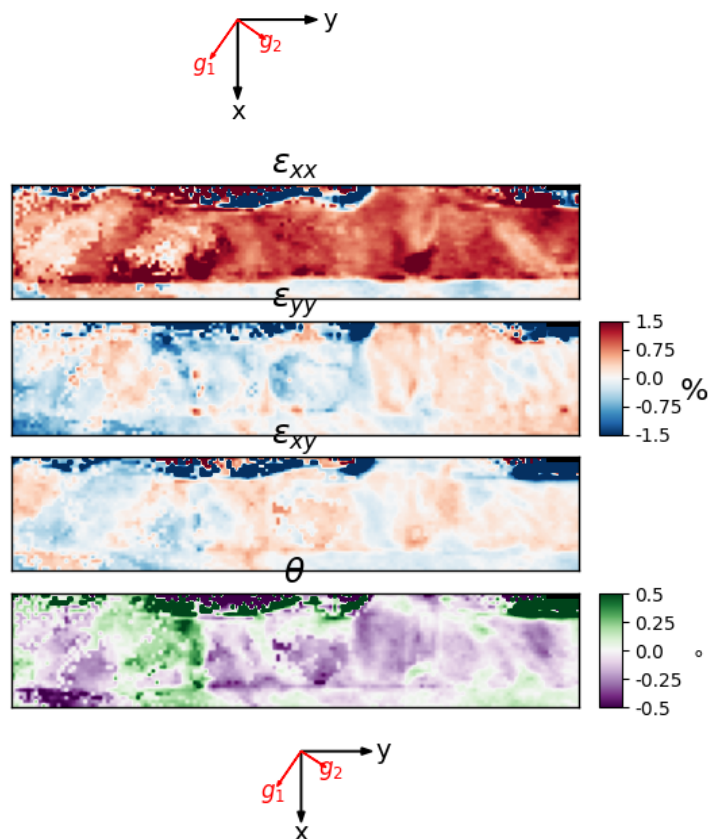


Figure S3: Strain maps for the LCMO film on LSAT for in ( $\epsilon_{yy}$ ) and out of plane ( $\epsilon_{xx}$ ) using vectors aligned with the image axes. The most notable feature is the large positive out-of-plane strain in this case. Most areas show strong negative deviations from perpendicular vectors ( $<90^\circ$ ) except one domain identified with the DDF imaging on the left.